Journal of Materials Science & Technology 80 (2021) 179–190

Contents lists available at ScienceDirect

Journal of Materials Science & Technology

journal homepage: www.jmst.org

Research Article

Erosion behavior and failure mechanism of Ti/TiAlN multilayer coatings eroded by silica sand and glass beads

Jintao Shuai[a,b], Xiao Zuo[a], Zhenyu Wang[a], Lili Sun[a], Rende Chen[a], Li Wang[a], Aiying Wang[a,b,c,*], Peiling Ke[a,b,c,*]

[a] *Key Laboratory of Marine Materials and Related Technologies, Zhejiang Key Laboratory of Marine Materials and Protective Technologies, Ningbo Institute of Materials Technology and Engineering, Chinese Academy of Sciences, Ningbo, 315201, China*

[b] *Center of Materials Science and Optoelectronics Engineering, University of Chinese Academy of Sciences, Beijing, 100049, China*

[c] *Ningbo Institute of Industrial Technology, Ningbo, 315201, China*

ARTICLE INFO

Article history:
Received 28 March 2020
Received in revised form 17 August 2020
Accepted 27 September 2020
Available online 5 January 2021

Keywords:
Ti/TiAlN multilayer coating
Erosion resistance
Microstructure
Failure mechanism

ABSTRACT

Severe erosion by hard particles is a crucial problem to engine blades when aircraft take off and land in harsh environments, especially for the developed lightweight titanium alloy components. Here, we deposited the Ti/TiAlN multilayer coatings with various cycles on Ti–6Al–4V substrates by a home-made hybrid multisource cathodic arc system. The effects of the silica sand and glass beads on erosion behavior of the coatings were focused. Results showed that the Ti/TiAlN multilayer coatings eroded by the silica sand exhibited the predominant "layer by layer" failure mechanism. In particular, increasing the number of cycles led to the dramatic increase in erosion rate for Ti/TiAlN multilayer coatings, due to the deterioration of their mechanical properties. Different from the silica sand case, however, the erosion rate of the coatings treated by glass beads indicated faint dependence upon the number of cycles, where the coating failure was dominated by the "piece by piece" failure mechanism. Noted that the Ti layers along with the formed interfaces enhanced the erosion resistance of the coatings, although the failure mechanisms were differently eroded by silica sand and glass beads. Meanwhile, the Ti layers and interfaces hindered the propagation of radial cracks and restrained the lateral cracks within one single TiAlN layer.

1. Introduction

Solid particles including sand, volcano ashes, ice pellets, salt crystals can be ingested into the engines with the compressed air when the aircraft take off or land. This generally causes severe erosion damage of the blades and vanes of aircraft engines, especially the first-stage blades made of titanium alloys [1–3]. In addition, such erosion leads to the geometry change and properties deterioration of the components such as blades and vanes, together with the high maintenance costs for systems. Depositing hard ceramic coatings on the surface of the metallic materials is considered as the most promising strategy, which enhances the erosion resistance of components in terms of modified mechanical properties [4–8]. Taking into account of the combined mechanical and tribological properties, the metal/ceramic multilayer coatings have drawn much attention as the protective coatings for engine parts recently. Moreover, those coatings possess a higher erosion resistance than that of the monolithic coatings, since the ductile metal layers can absorb impacting energy by inducing plastic deformation, while the hard ceramic layers provide the resistance to wear [9,10]. Furthermore, the formed interfaces can deflect and even suppress the propagation of cracks, which slow down the development of erosion. Alternatively, Ti/TiAlN multilayer coatings were mostly investigated due to their comprehensive performances like high hardness, superior load capacity and excellent crack resistance, showing great potential as wear- and erosion-resistant coatings [11–14].

The architecture of the multilayer coatings, like the thickness ratio and the number of cycles, plays a vital role in their erosion resistance. For example, Wieciński et al. [10] found that the thickness ratio of the Cr/CrN multilayer coatings strongly affected their erosion resistance, and the coating with optimal thickness ratio had an extremely low volume loss, which was about 150 times lower

---

* Corresponding authors at: Key Laboratory of Marine Materials and Related Technologies, Zhejiang Key Laboratory of Marine Materials and Protective Technologies, Ningbo Institute of Materials Technology and Engineering, Chinese Academy of Sciences, Ningbo, 315201, China.

E-mail addresses: aywang@nimte.ac.cn (A. Wang), kepl@nimte.ac.cn (P. Ke).

https://doi.org/10.1016/j.jmst.2021.01.001
1005-0302/

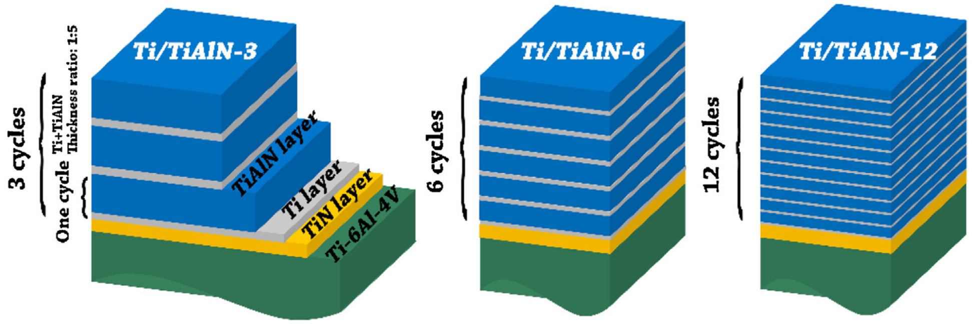

Fig. 1. Structural diagram of Ti/TiAlN multilayer coatings with different cycles.

than that of the uncoated samples. Lin et al. [15] investigated the sand erosion properties of TiN/Zr/ZrN multilayer coatings with different cycles, results showed that the coatings with the 96 cycles possessed the higher erosion resistance than that of the coatings with fewer cycles. Whereas, Cao et al. [16] found that the erosion resistance of multilayer coatings decreased with the number of cycles against the sand particles.

The property of the erosion particle is another key factor for the erosion resistance of the multilayer coatings. Borawski et al. [17] studied the effect of the coating architecture on erosion performance of the coatings. They suggested that the two-layer Ti/TiN multilayer coating owned the best erosion performance against the hard alumina particles, whereas coatings with 32 layers (16 each of TiN and Ti) offered the best erosion performance against the soft glass beads.

Till now, great efforts have been attempted to improve the erosion resistance of metal/ceramics multilayer coatings. However, the effect of the number of cycles on the erosion performance of multilayer coatings has not been fully understood yet. Besides, the effects of the metal layers and the formed interfaces within the multilayer coatings are still unclear, lacking direct evidence from the detailed characterization and observation. In addition, if one keeps the mind that the aircraft frequently operate in different environments, there is still a paucity of data concerning the erosion resistance of multilayer coatings eroded by various kinds of particles in practical application.

In this study, Ti/TiAlN multilayer coatings with different cycles of 3, 6, 12, 24 and 72 were deposited on Ti–6Al–4V substrates by a home-made hybrid multisource cathodic arc ion deposition system. The effect of the silica sand and glass beads on erosion behavior of the multilayer coatings was focused. Particularly, the failure mechanism of coatings was discussed in terms of the structural evolution dependence upon ductile metal layers and interfaces. The results here can provide a fundamental understanding of enhanced erosion resistance by multilayer coating architecture, and bring forward an alternative strategy to fabricate the coating materials for aircraft components used in harsh environments.

2. Experimental

2.1. Coating deposition

Titanium alloy of Ti–6Al–4V with a dimension of $15 \times 15 \times 3\,\text{mm}^3$ was employed as substrates. All substrates were grounded down to 5000 grit by SiC abrasive papers and ultrasonically cleaned in ethanol for 20 min before the deposition process. The Ti/TiAlN multilayer coatings were fabricated by a home-made hybrid multisource cathodic arc ion deposition system [9]. The base pressure of the chamber was 3×10^{-3} Pa and heated to 300 °C before the deposition process. Ti target with the purity of 99.9 wt.% and TiAl target in an atomic ratio of 33:67 were applied as cathodes to deposit the Ti/TiN layers and TiAlN layers, respectively. Before deposition, the substrates were etched by an Ar ion beam source for 30 min at a pressure of 0.27 Pa with a DC pulsed negative bias of 100 V. To enhance the coating adhesion strength to substrates, the Ti ions bombardment was performed for 8 min with a substrate bias of −500 V. Subsequently, a TiN interlayer with a thickness of about 700 nm was prepared with a substrate bias of −60 V at the pressure of 1.6 Pa. Then the Ti and TiAlN layers were alternately deposited by controlling the gas supply of Ar/N_2 and the arc power of targets. During the Ti (named as the bottom layer) and TiAlN (named as the top layer) deposition, the substrate was supplied with the bias of −80 V. The working cathodic current for Ti and TiAl targets were both set at 70 A, and the substrate holder rotated during the deposition process for the uniformity. The total thickness was kept around 11 μm for all multilayer coatings, and the thickness ratio of one TiAlN layer to one Ti layer was 1:5. Namely, one Ti layer and one TiAlN layer were defined as one cycle and the number of cycles was 3, 6, 12, 24 and 72, corresponding to the sample of Ti/TiAlN-3, Ti/TiAlN-6, Ti/TiAlN-12, Ti/TiAlN-24 and Ti/TiAlN-72, respectively. Fig. 1 shows the structural diagram of the Ti/TiAlN-3, Ti/TiAlN-6 and Ti/TiAlN-12 as examples. Detailed deposition parameters of the coatings are presented in Table 1.

2.2. Characterization techniques

Scanning electron microscopy (SEM, FEI Quanta FEG 250, USA) was applied to observe the surface and cross-sectional morphology of the as-deposited and the eroded Ti/TiAlN multilayer coatings, as well as the morphology of scratch tracks. The chemical composition of the erodent was determined with the energy-dispersive X-ray spectroscopy (EDS) at an accelerating voltage of 20 kV. The cross-sectional eroded samples were cut by a low-speed saw (IsoMet^{TM}, Buehler, USA), then polished by a broad ion beam system (BIB) using Leica EM TIC 3X at the voltage of 7 kV, fundamental of BIB technique can be found in Ref. [18]. The crystal structure of the as-deposited Ti/TiAlN multilayer coatings was analyzed by X-ray diffraction (XRD, Bruker D8 Advance, Germany) with a diffractometer using Cu K_α radiation (wavelength 1.5406 Å). All measurements were performed using detector scanned in a 2θ range of 30°–90°, and the step size was 0.02° with a scanning rate of 5°/min at 40 kV and 40 mA. X-ray photoelectron spectroscopy (XPS, Axis Ultra DLD, Japan) was utilized to characterize the chemical composition of the multilayer coatings, while their constituent bonds were identified using monochromatic Al K_α irradiation at pass energy of 160 eV. Three measurements were conducted in random areas. To avoid the influence of the surface contamination, the analyzed spots were cleaned by Ar ions of 2 keV for 2 min before measurement.

The hardness and elastic modulus of the as-deposited coatings were determined using nanoindentation (NanoIndentation G200, MTS, USA) with a Berkovich-diamond tip in continuous stiffness

Table 1
Process parameters of the Ti/TiAlN multilayer coatings.

	Ti/TiAlN-3	Ti/TiAlN-6	Ti/TiAlN-12	Ti/TiAlN-24	Ti/TiAlN-72
Temperature (°C)	300				
Targets current (A)	Ti layers– Ti: 70, TiAlN: 0 TiAlN layers– Ti: 0, TiAlN: 70				
Bias voltage (V)	Ti and TiAlN layers: −80				
Pressure (Pa)	Ti layer– 2.7 (Ar), TiAlN layer– 6.7 (N_2)				
Deposition time for each layer (min)	Ti: 10 TiAlN: 76	Ti: 5 TiAlN: 38	Ti: 2.5 TiAlN: 19	Ti: 1.25 TiAlN: 9.5	Ti: 0.4 TiAlN: 3.1

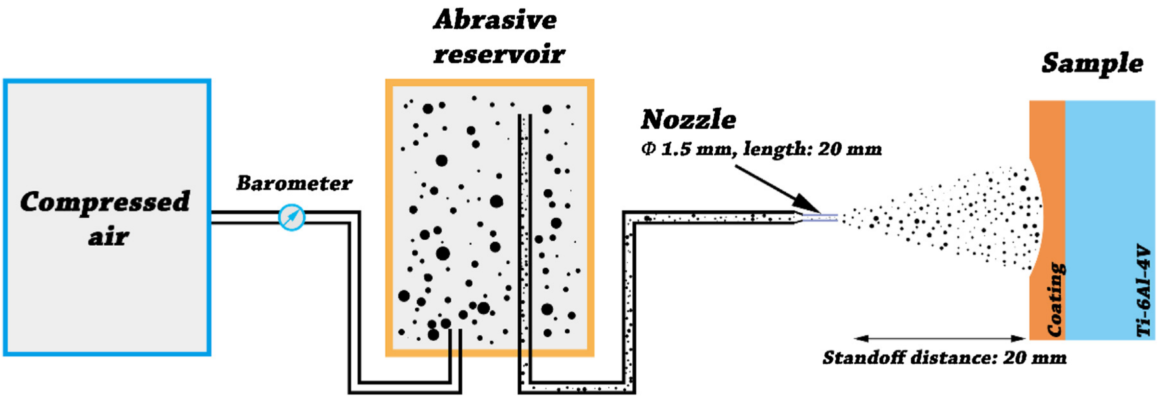

Fig. 2. Schematic diagram of the erosion test rig.

measurement (CSM). The representative hardness of the coatings was selected in the depth of 500 nm (less than 1/10 of the coatings' thickness) to avoid the effect caused by the substrates [19]. Considering the influence of metallic macroparticles of the coatings on the evaluation of hardness, samples were polished by ball-cratering apparatus with a 2-cm-radius steel ball for a few seconds before the tests. Twelve random indents were performed on each sample. The values of hardness and elastic modulus were calculated following the model of Oliver and Pharr [20]. A Poisson's ratio of 0.25 was assumed for all coatings [9].

The adhesion strength of the coatings to the substrates was determined by scratch tests using CSM Revetest (Switzerland) equipped with a diamond Rockwell conical indenter (an apex angle of 120° and a curvature radius of 200 μm). The indenter was loaded continuously from 0 to 150 N at the speed of 1.5 mm/min for 3 mm. At least three tests for each sample were conducted to acquire solid results.

2.3. Erosion test

The erosion tests were performed at room temperature by a home-made test rig concerning the ASTM G76−13 standard. The schematic diagram of the tester is shown in Fig. 2. The test rig consists of three major parts: (1) the air supply system which can provide compressed air with different pressure within the range of 0.1–1 MPa (0.2 MPa was employed in this study). (2) the abrasive reservoir which stores erodent and ensures the total dosage of erodent for each test was equal. (3) the blasting system includes the acceleration nozzle (tungsten carbide, *Φ* 1.5 mm, length: 20 mm) and sample fixture (impact angle: 90°). The distance between the sample and the nozzle was 20 mm. The particles are dispersed in the reservoir by the compressed air flow and gain high kinetic energy through the acceleration nozzle toward the specimen.

Angular silica sand (~61 μm) and spherical glass beads (~106 μm) were used as erodent. Fig. 3 shows the morphology, chemical composition, and size distribution (measured by laser particle size analyzer, HELOS H3938, Germany). As the density of the silica sand was lower than that of the glass beads, the feed rates of the silica sand and glass beads were 2 ± 0.5 g/min and 5 ± 1 g/min, respectively. Since the hard particles with irregular sharp edges generally caused more damage to a surface than soft spherical particles, the total doses of the silica sand and the glass beads were set at 10 g and 50 g, respectively.

The erosion rate was determined according to the Eq. (1). Mass loss of the specimen was the mass change before and after the erosion test, which was determined by an analytical balance with a resolution of 0.01 mg (Mettler Toledo, XS205 DU). Samples were ultrasonically cleaned with ethanol for 15 min to remove impurities and residual erodent before and after the erosion tests, then dried by high-pressure nitrogen. At least three tests for each sample were conducted to enhance the quality of statistics.

$$\text{Erosion rate (ER)} = \frac{\text{Mass loss of the specimen (mg)}}{\text{Dosage of particles (g)}} \tag{1}$$

3. Results and discussion

3.1. Crystal structure and chemical composition

To investigate the phase structure of the as-deposited Ti/TiAlN multilayer coatings with different cycles, X-ray diffraction was conducted. As shown in Fig. 4, the patterns of Ti/TiAlN multilayer coatings revealed peaks corresponding to the (111), (200), (220), (311) planes for the TiAlN phase. Another set of diffraction peaks could be signed to the (100), (002), (101), and (102) four crystal planes of the pure Ti phase. Noted that increasing the number of coating cycles, the intensity of the TiAlN (001) generally decreased, while the intensities of TiAlN (200), (220), (311) diffraction peaks barely changed. During the deposition process, TiAlN usually preferred to form (111) plane due to the high internal stress. But the induced Ti layers interrupted the continuous growth of the TiAlN, reducing the internal stress. Thus, the intensity of the TiAlN (111) plane decreased with the increasing number of cycles, and the intensity of the (200) remined relatively high. The intensities of the Ti phase with (100) and (101) peaks decreased slightly. Con-

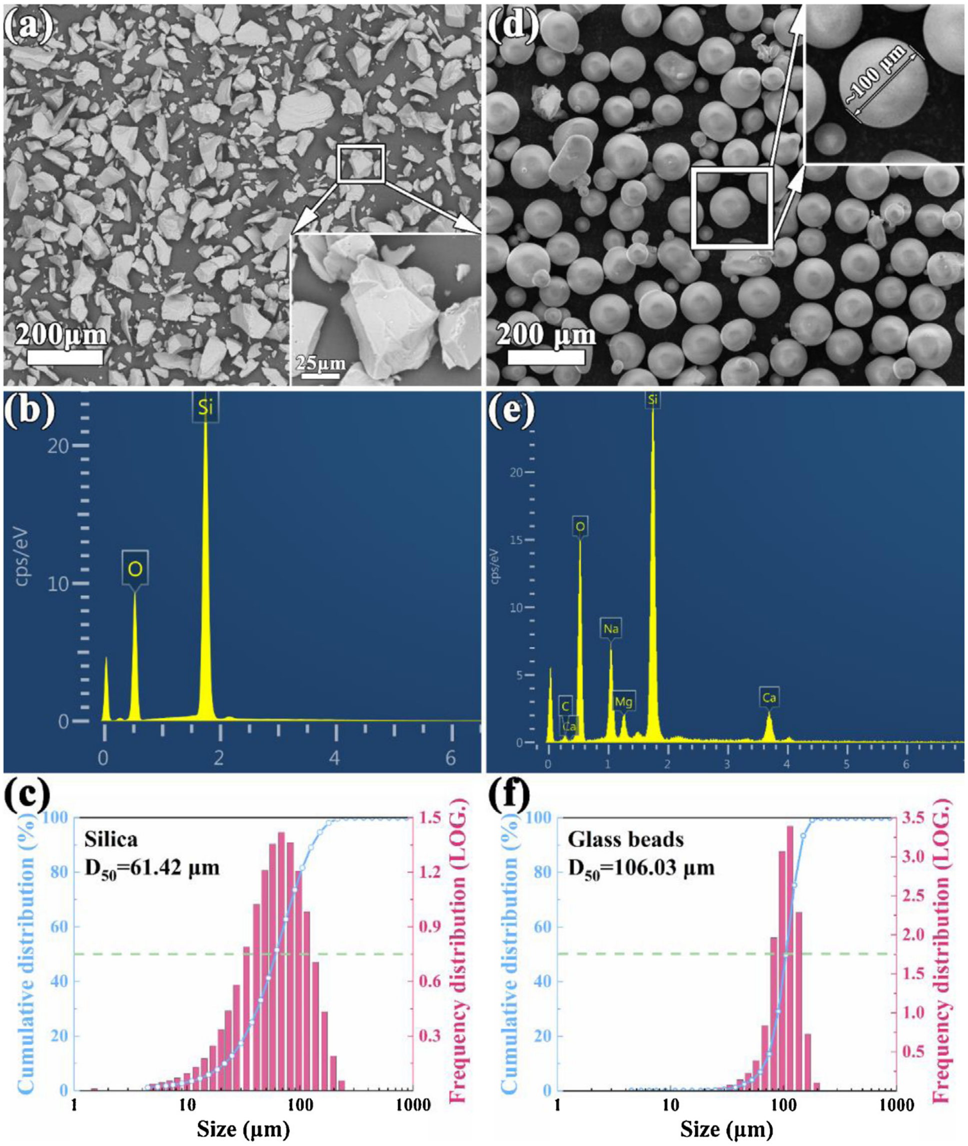

Fig. 3. (a, d) Morphology, (b, e) chemical composition and (c, f) size distribution of the silica sand and the glass beads, respectively.

Table 2
Chemical composition of the Ti/TiAlN multilayer coatings. (at.%).

Sample	Ti	Al	N
Ti/TiAlN-3	18.67 ± 0.17	31.29 ± 0.25	50.04 ± 0.32
Ti/TiAlN-6	17.85 ± 1.03	32.92 ± 0.74	49.23 ± 0.67
Ti/TiAlN-12	18.45 ± 0.51	32.30 ± 1.96	49.25 ± 1.47
Ti/TiAlN-24	17.33 ± 0.87	33.68 ± 2.07	48.99 ± 1.92
Ti/TiAlN-72	17.73 ± 0.91	32.63 ± 0.24	49.63 ± 0.67

sidering the N_2 was used to deposit TiAlN layers while Ar gas was introduced for deposition of the Ti layer, a trace amount of residual nitrogen in the chamber could exist after switching the N_2 flow to Ar flow. As a consequence, TiN_{1-x} can be formed at the initial stage of the Ti layer deposition process [21,22]. Such an increase of formed TiN_{1-x} phase with the increase of coating cycles would be the reason for the decline of the total thickness in the pure Ti layer, which finally led to the decrease of representative peaks of the Ti phase.

Table 2 shows the chemical compositions of the multilayer coatings determined by XPS. The results showed that the atomic concentrations of the Ti (~18 at.%), Al (~32 at.%) and N (~50 at.%) were similar for each coating, which represented that the atomic concentration of top layers did not change with the number of cycle of the multilayer coatings. Fig. 5 shows the Ti 2p, Al 2p, and N 1s XPS spectra from the surfaces of the Ti/TiAlN multilayer coatings. According to Fig. 5(a)-(c), no significant changes can be found in the Ti 2p, Al 2p, and N 1s XPS spectra with the increasing number of cycles. This was due to the surface of the coatings were all TiAlN layers, and the deposition conditions were the same. In order to obtain the bond arrangements, the XPS spectra of Ti 2p, Al 2p, and N 1s of the Ti/TiAlN-6 were selected to analysis (Fig. 5(d)-(f)). Fig. 5(d) shows the Ti 2p peaks at 455.2 eV (Ti 2p3/2) and 461.2 eV (Ti 2p1/2), which can be assigned to Ti—N bond [23], peaks at 457.1 eV (Ti 2p3/2) and 463.1 eV (Ti 2p1/2) are characteristic of Ti—O bond [24]. Fig. 5e shows the Al peak at 74.3 eV corresponding to Al—N bond [25] and a very week signals at 74.7 eV corresponds to Al—O bond [25]. The source of O should be the trace residual oxygen in the chamber prior the deposition process. Fig. 5f shows the N 1s spectrum recorded from Ti/TiAlN-6, which is characterized by quite a symmetrical peak centered around 396.9 eV. This binding energy is close to that reported by Marco (396.8 eV) for Ti-N bond [25]. A small peak can be observed at the bonding energy of 398.3 eV, which can be Al-N bond [26].

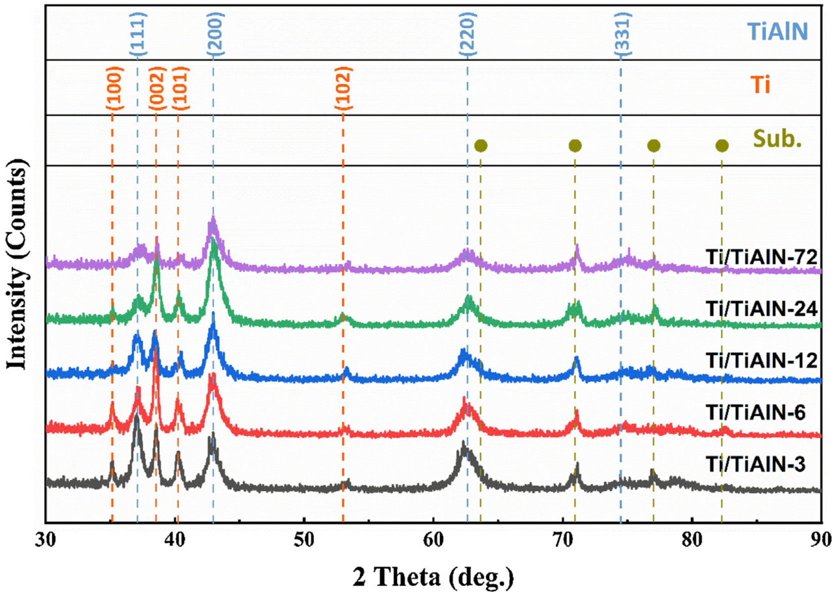

Fig. 4. XRD patterns of the Ti/TiAlN multilayer coatings.

3.2. Mechanical properties

Mechanical properties of ceramic coatings play an important role in erosion resistance of the coatings [27–30]. Fig. 6a shows the hardness (*H*) and elastic modulus (*E*) of the Ti–6Al–4V substrate and the Ti/TiAlN multilayer coatings determined by the nanoindentation. The hardness and elastic modulus of the coated samples were at least 2–3 times higher than those of the substrate (4.7 ± 0.7 GPa and 142.7 ± 14.3 GPa, respectively). According to our previous work [9], the hardness and elastic modulus of the monolithic TiAlN coating with a similar thickness were ~35 GPa and ~367 GPa, respectively. Ti/TiAlN multilayer coating with 3 cycles exhibited a similar hardness and a higher elastic modulus of 33.9 ± 1.1 GPa 424.1.0 ± 22.6 GPa, respectively. With increasing the coating cycle from 3 to 72, the elastic modulus of the coatings gradually dipped 326.5 ± 2.2 GPa, whereas the hardness decreased significantly to 19.1 ± 0.4 GPa. This could be understood in terms of the lower hardness of the Ti layer than that of the TiAlN layer. Increasing the coating cycle benefited the soft and ductile Ti layer with well-distribution along the direction of coating thickness, which lowered the total hardness of multilayer coatings [7].

It is empirically known that the H/E ratio quantified the elastic strain to failure [2,31], and the H^3/E^2 ratio represented resistance to plastic deformation [31–34], which comprehensively control the erosion phenomena of materials. As illustrated in Fig. 6(b), the coated samples exhibited the higher value of H/E and H^3/E^2 (higher than 0.05 and 0.05 GPa, respectively) than those of the uncoated sample (0.033 and 0.141 GPa, respectively). This gave the clue that the coatings could improve the erosion resistance of titanium alloy as expected. As the number of cycles increased, the H/E ratio declined slightly from 0.079 to 0.059, but the H^3/E^2 ratio fell significantly from 0.217 GPa to 0.065 GPa. Given the fact that the Ti/TiAlN-3 exhibited the best mechanical properties (the highest hardness, elastic modulus, H/E, and H^3/E^2) among other coatings, the erosion resistance of the Ti/TiAlN-3 was expected to be the best.

Fig. 7 shows the adhesion strength of the coatings and their scratch tracks' morphology. The adhesion strength (i.e. critical load) was defined as the load corresponded to the complete and continuous delamination events with large area exposure of the substrate. As shown in Fig. 7a, all coatings (expecting the Ti/TiAlN-72) exhibited a good adhesion strength with a minimum critical load of higher than 100 N. The good adhesion strength of these coatings could be explained by the presence of the Ti layers and interfaces [9]. As cycles were increased from 3 to 24, the value of the critical loads gradually decreased from 122.0 ± 5.6 N to 101.0 ± 10.5 N, while dropped significantly to 64.7 ± 5.5 N for Ti/TiAlN-72, which was attributed to the decline of mechanical properties and crack resistance [35,36]. In addition, the thickness of one single Ti layer decreased with the increasing number of cycles, thus, the absorbing energy and hindrance effects of the titanium layers decreased, weakening the crack resistance of the coatings, although the number of the interfaces also increased.

Observing the morphology of the scratch track is also a powerful method to qualitatively evaluate the toughness of coatings [37,38]. At loads of approximately 130 N and 120 N, the substrate of the Ti/TiAlN-3 and Ti/TiAlN-6 started to be visible (Fig. 7(b)–(c)). Only a few small debris can be seen at the edge of the track (Fig. 7(g)–(h)) and no obvious chipping events can be found, revealing a good toughness of the coating. As the number of cycles increased to 12, the substrate exposed at about 110 N (Fig. 7(d)). Meanwhile, the cohesive failure occurred at the edge of the scratch track (Fig. 7(i)). This indicated the crack resistance of the Ti/TiAlN-12 was lower than that of the Ti/TiAlN-6. The load of the cohesive failure of the Ti/TiAlN-24 (~80 N, Fig. 7(e)) was lower than its critical load (~100 N, Fig. 7(e)), where the severer chipping events emerged at the edge of the tracks, suggesting the poorest crack resistance of the Ti/TiAlN-24. However, adhesion strength dropped significantly when the number of cycles increased to 72 (Fig. 7(f)), and peel-off event occurred at the load of ~40 N and existed along the direction of the scratch track, representing the poorest crack resistance of the Ti/TiAlN-72(Fig. 7(k)). According to our previous results, compared with the TiAlN monolithic coatings, Ti/TiAlN multilayer coatings showed a higher crack resistance. Since the Ti layers served as the glue bonding the brittle and hard TiAlN layers, which led to the enhanced crack resistance of multilayer coating [9]. Besides, Ti layers could coordinate the deformation between the substrate and the TiAlN layers and absorb energy by inducing plastic deformation. And the formed interfaces could hinder the propagation of

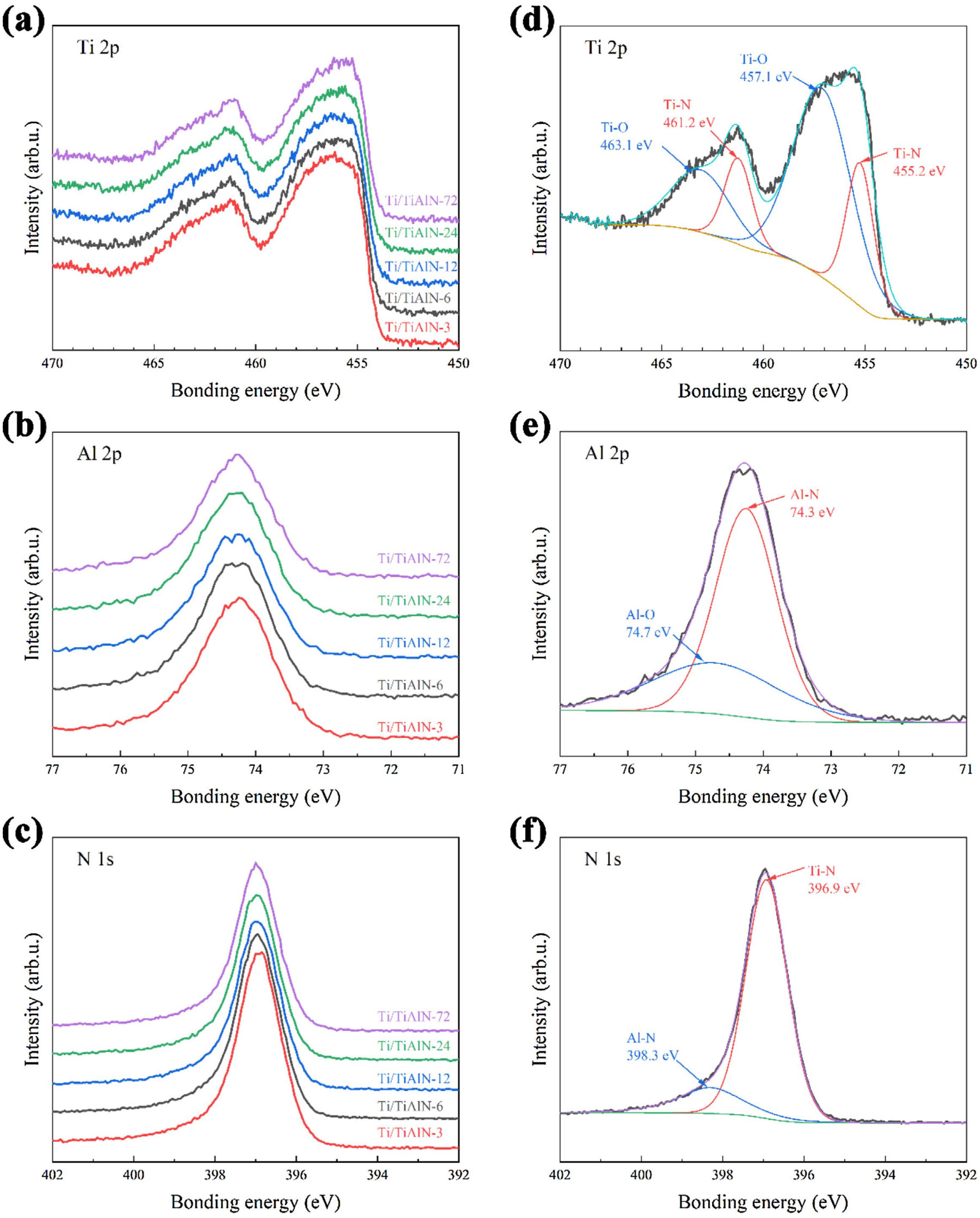

Fig. 5. XPS spectra of Ti/TiAlN multilayer coatings: (a) Ti 2p (b) Al 2p (c) N 1s and XPS spectra fitting results of Ti/TiAlN-6: (d) Ti 2p (e) Al 2p (f) N 1s.

the cracks in the TiAlN layers. However, as the cycles increased, the number of interfaces increased and the Ti layers distributed more uniformly along the direction of coating thickness. As a consequence, the decreased hardness lowered the scratch resistance of the coatings. Besides, the decreased thickness in the single Ti layer reduced the plastic deformation of the Ti layer. The large amount of interfaces and excessively thin Ti layers led to the poor crack resistance of the coatings. In this regard, the feature of the Ti layer and interfaces played a key role in the evolution of crack resistance of coatings, particularly the Ti layer was the predominated factor comparing with the effect of interfaces.

3.3. *Erosion resistance*

Fig. 8 illustrates the erosion rates of pristine Ti–6Al–4V substrates and the Ti/TiAlN multilayer coatings eroded by silica sand and glass beads. Regardless of the erosion particles, all coatings presented the lower erosion rate than that of the pristine alloy substrate due to the improvement of the mechanical properties of coatings. Noted that, however, the significant substrate erosion contributed to the evaluation of erosion rate of coatings, because the substrate mostly exposed in severe erosion tests. Fig. 8(a) shows the erosion rates of the substrate and coatings eroded by silica sand.

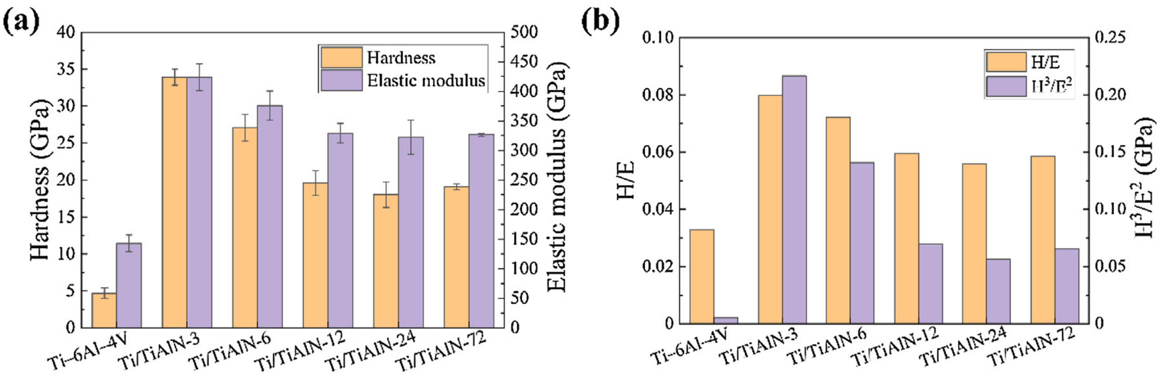

Fig. 6. (a) Hardness and elastic modulus and (b) H/E and H^3/E^2 ratios of the Ti–6Al–4V substrate and the Ti/TiAlN multilayer coatings.

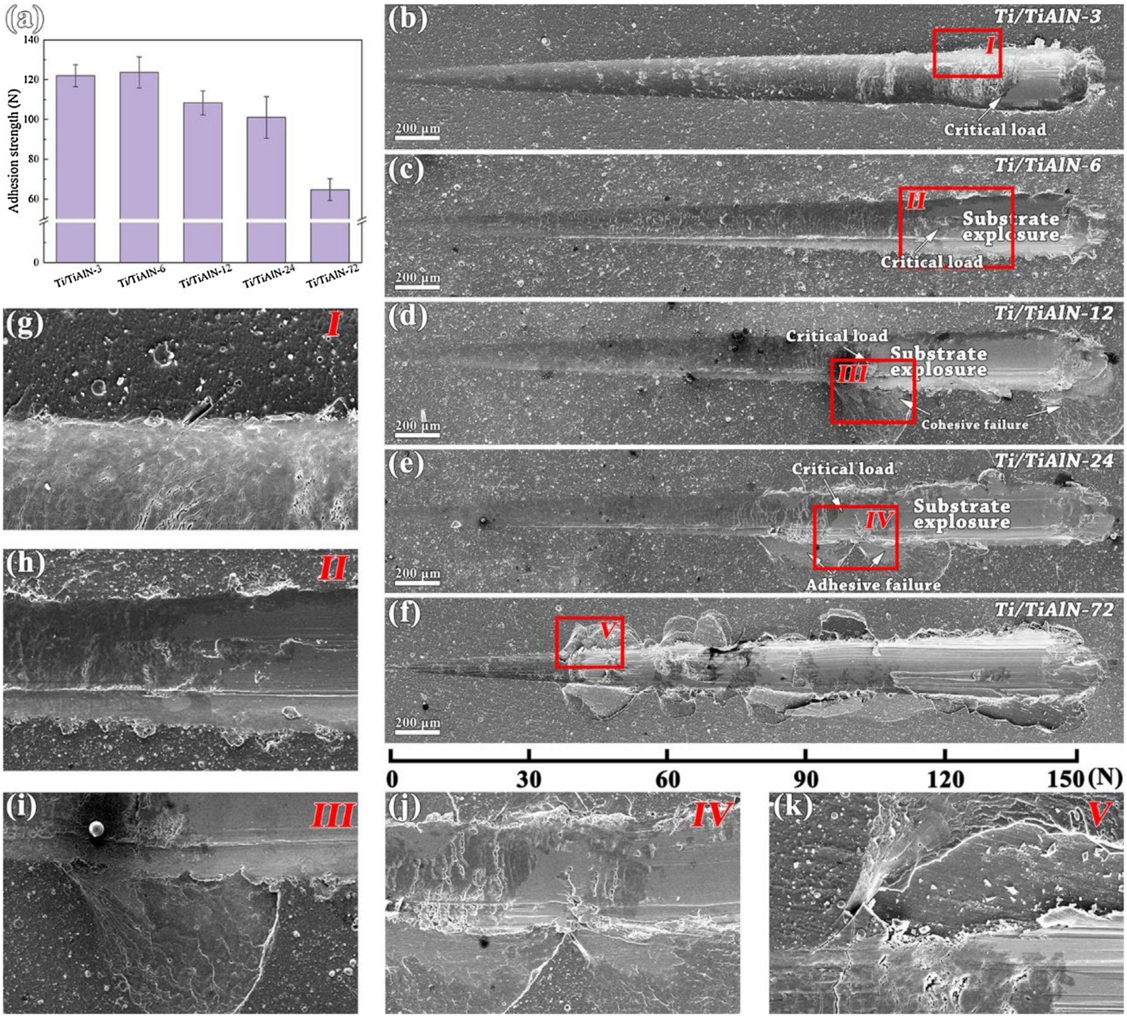

Fig. 7. (a) Adhesion strength, (b)–(f) scratch morphology of the Ti/TiAlN multilayer coatings and (g)–(k) enlarged images of the framed area in Fig. 7(b)–(f), respectively.

The erosion rate of the substrate was 0.55 ± 0.013 mg/g, which was approximately 19 times higher than that of the Ti/TiAlN-3 (0.029 ± 0.005 mg/g). While increasing the coating cycle from 3 to 72, the erosion rate of the coatings dramatically went up to 0.385 ± 0.002 mg/g. According to our experimental results, the erosion rate of the TiAlN monolithic coating eroded by silica sand was 0.034 ± 0.013 mg/g, which was higher than that of the Ti/TiAlN-3. Different from the strong erosion ability of the silica sand [39], both the erosion rate of the substrate and coatings by glass beads decreased one order of magnitude. As shown in Fig. 8b, the erosion rate of the substrate was only 0.028 ± 0.002 mg/g, which was about twice as much as that of the coatings. Meanwhile, the erosion rate of the coatings (Ti/TiAlN-3 to Ti/TiAlN-24) kept almost constant (~0.01 mg/g), regardless of the increase in the number of cycles. When the number of the cycles increased to 72, the erosion rate of the Ti/TiAlN-72 went up slightly to 0.0173 ± 0.002 mg/g. Comparing the erosion behavior with silica and glass beads, it could be said that the hard silica sand with sharp edges as erosion particles showed the stronger damage effect of the erosion resistance of protective coatings than that with soft spherical glass beads.

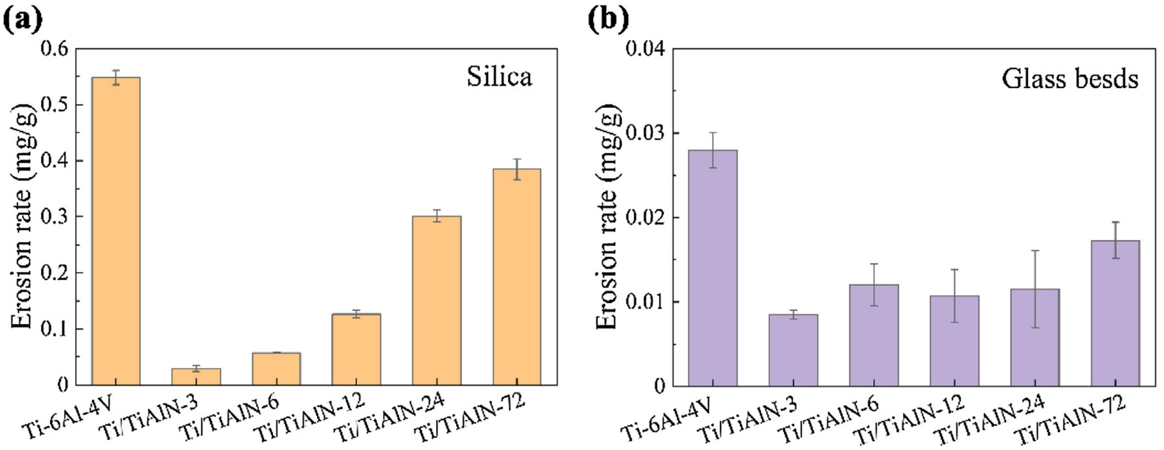

Fig. 8. Erosion rate of the Ti–6Al–4V substrate and the Ti/TiAlN multilayer coatings eroded by (a) silica sand and (b) glass beads.

3.4. *Erosion behavior of the Ti/TiAlN multilayer coatings*

To reveal the erosion mechanism of Ti/TiAlN multilayer coatings related to various erodent particles, further structural evolution including surface morphology and cross-sectional images were observed.

3.4.1. *Silica sand as erodent*

Fig. 9 shows the damage evolution of the Ti/TiAlN-6 eroded by the angular silica sand. As shown in Fig. 9(a), the as-deposited coating exhibited a compact microstructure, although some metallic macroparticles and micro pits could be observed at the surface, which was typical features of coatings prepared by cathodic arc ion deposition [40–42]. The metallic macroparticles were mainly attributed to the ejected liquid droplets from the target during arc discharge, while the formation of the micro pits mainly raised from the spallation of some large particles during the deposition process [15,43,44]. At the initial stage (Fig. 9(b)) of the erosion, a large amount of the macroparticles peeled off, because of the repeated impacting and remained many micro pits at the surface of the coating. Ring cracks presented around micro pits (Fig. 9(c)) followed by their propagation as the erosion lasting, which decreased the cohesive strength of the coating. Thus, a small part of the coating spalled off (Fig. 9(d)) and the dimension of the micro pits enlarged (Fig. 9(e)) accompanying the newly formed ring cracks. The above process would be repeated if the erodent continuously impacted the samples, and many micro pits extended and coalesced into a larger erosion scare. Finally, the coating was exhausted and the substrate exposed (Fig. 9(f)), the coating would lose the protection benefits. It should be noted that the multilayer coatings eroded by silica sand exhibited the “layer by layer” failure mechanism (Fig. 9(c) and (e)), which was a typical damage feature of the multilayer coatings [10,45].

Fig. 10(a) illustrates the cross-sectional morphology of the as-deposited Ti/TiAlN-6, revealing the well-defined compositional modulation consisted of alternate brighter Ti layers and darker TiAlN layers. No cracks or defects could be found, except for a small number of metallic macroparticles. As the silica sand impacted the surface of the coating, the top layer of the TiAlN was removed gradually (Fig. 10(b)). A few radial cracks were visible at the edge of the eroded area. However, no radial or lateral cracks was produced at other layers of the coating. Fig. 10(c) shows the enlarged image of the framed area in Fig. 10(b). Radial cracks initiated at the surface of the coating and propagated toward the substrate, yet they were hindered by the Ti layer. Then the newly exposed TiAlN layer was under impact by the erodent directly and removed gradually (Fig. 10(e)). Because of the contribution of the Ti layers to the radial cracks, the coating showed the nature of the “layer by layer” failure mechanism (Fig. 10(d)). However, it should be mentioned that plastic deformation might occur at the substrate (Fig. 10). The reason was that a small part of the erodent’s kinetic energy was transferred from coating to substrate, and the substrate absorbed the energy by plastic deformation, especially when the coating was partially eroded. Since the plastic deformation occurred at the substrate, radial cracks generated at the TiN interlayer and propagated towards the surface of the coating, yet the radial cracks were deflected at the interfaces of the Ti layer and TiAlN layer.

To conclude, the erosion damage of the Ti/TiAlN multilayer coatings treated by the angular silica sand commonly began at the defects of the coatings (metallic macroparticles). Those sites were the vulnerable regions of the mechanical properties, which would easily become the initiation of the erosion damage. The spallation of the macroparticles remained micro pits at the surface of the coatings, whose dimension could further extend under the continuous erosion process. Those pits coalesced with each other, leading to the failure of the coatings. The erosion damage evolution of Ti/TiAlN multilayer coatings exhibited the typical “layer by layer” mechanism. The presented Ti layers and formed interfaces could deflect or even suppress the propagation of the radial cracks.

3.4.2. *Glass beads as erodent*

Fig. 11 illustrates the erosion behavior of the Ti/TiAlN-6 eroded by the spherical glass beads. A few short cracks were observed within a macroparticle at the beginning (Fig. 11(a)). Metallic macroparticles spalled off due to the propagation of the cracks (Fig. 11(b)), followed by the formation of the ring cracks around the micro pits (Fig. 11(c)). Ring cracks further propagated under the repeated erosion actions, which promoted the formation of the squamous cracks around the pits (Fig. 11(d)). The poor adhesion strength of the coating around the pits further triggered the removal of the coating and enlarged the dimension of the pit (Fig. 11(e)). Meanwhile, ring cracks were generated again and further propagated as long as the erosion process continued. As a consequence, many pits emerged with each other, leading to the failure of the coating and the exposure of the substrate (Fig. 11(f)). Unlike the damage evolution of the coatings under the erosion of the silica sand, coatings under the erosion of the glass beads exhibited the “piece by piece” failure mechanism. To the best knowledge of the authors, this phenomenon was firstly reported in this multilayer coating subjects.

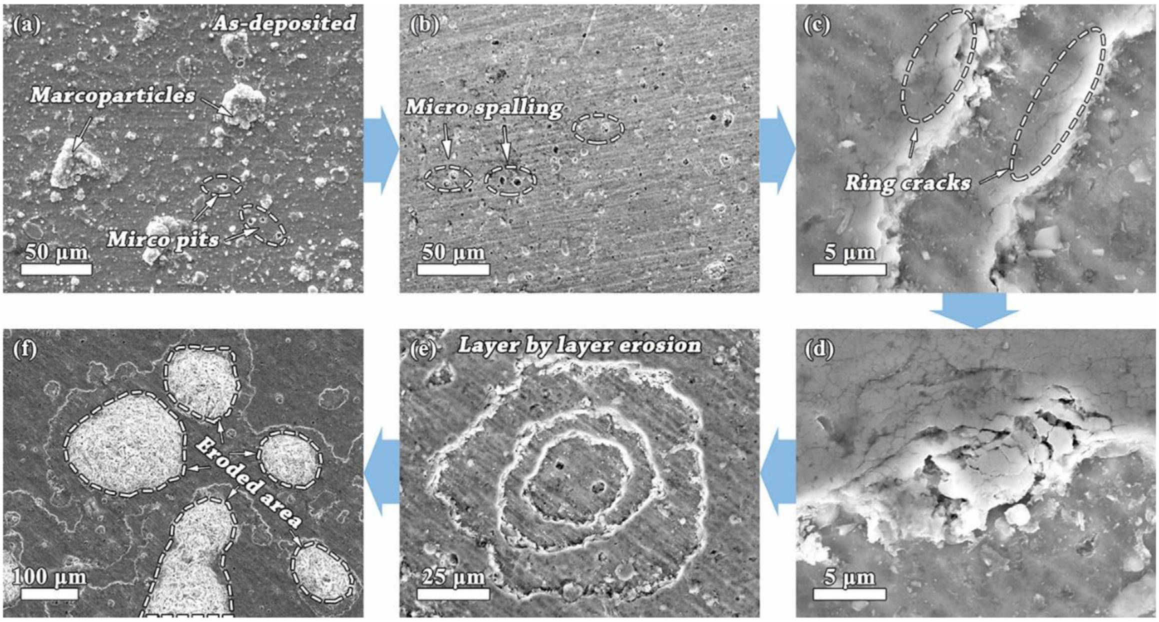

Fig. 9. Erosion behavior of the Ti/TiAlN-6 eroded by silica sand. SEM image of (a) surface morphology of the as-deposited coating, (b) micro spalling, (c) ring cracks, (d) propagated ring cracks, (e) layer by layer erosion and (f) erosion scares.

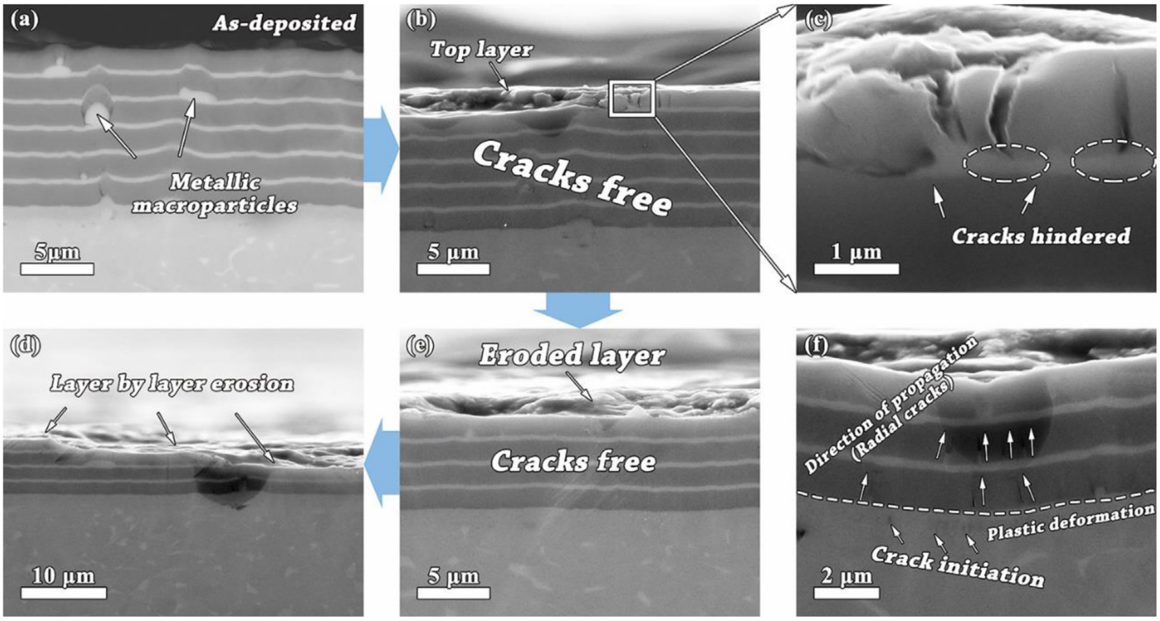

Fig. 10. Cross-sectional morphology of the Ti/TiAlN-6 eroded by silica sand. SEM image of (a) cross-sectional morphology of the as-deposited coating, (b) erosion at the top TiAlN layer, (c) enlarged image of the framed area in (b), (d) layer by layer erosion, (e) erosion at the second TiAlN layer and (f) plastic deformation at the substrate.

Fig. 12 shows the cross-sectional morphology of the Ti/TiAlN-6 eroded by glass beads. The morphology of the cross-sections showed the nature of the brittle fracture, delamination can be observed near the interface of the coating and the substrate (Fig. 12(a)). As illustrated in Fig. 12(b), the erosion scare can be divided into three zones: (1) the eroded area, where the coating was exhausted and the substrate was exposed. (2) the radial and lateral cracks zone consisted of many radial cracks and a few lateral cracks, and (3) the lateral crack propagation zone. The lateral cracks were induced by the delamination between the coating and the substrate, as shown in Fig. 12. Fig. 12(c) was the enlarged image of the radial and lateral cracks zone, radial cracks were generated at the surface of the coating and spread towards the substrate, but they were deflected at the interfaces between the Ti layers and TiAlN layers. Besides, the Ti layers deflected the propagation of the lateral cracks, limiting the lateral cracks within a single TiAlN layer (Fig. 12(d)). Meanwhile, the kinetic energy of the erodent was transferred to the substrate from the coating after impacting the samples since the glass beads were blunt without sharp edges. In addition, the titanium alloy absorbed the energy by plastic deformation (Fig. 12(e)). Once the amount of the plastic deformation exceeded the toughness of the coating, cracks even delamination would occur at the interface of the coating and the substrate (Fig. 12(a) and (b)). Cracks and delamination would further develop, and the coating was removed gradually with the erosion lasting.

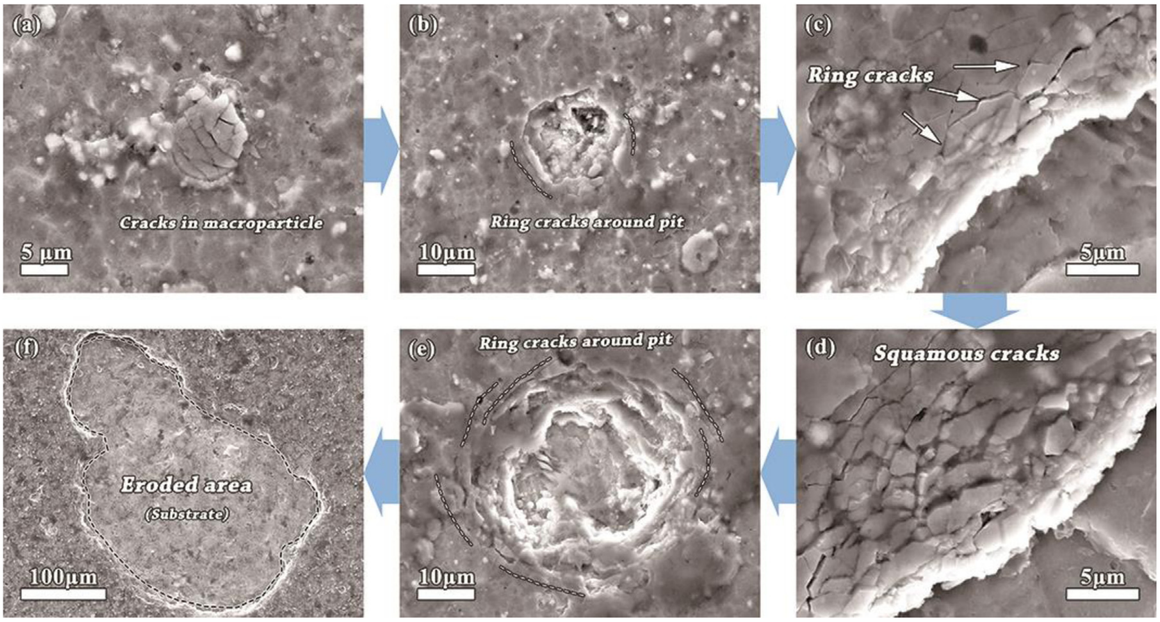

Fig. 11. Erosion behavior of the Ti/TiAlN-6 eroded by glass beads. SEM image of (a) cracks in the macroparticle, (b) ring cracks around the pit, (c) propagated ring cracks, (d) squamous cracks, (e) development of the pit and (f) erosion scares.

Overall, the failure of the Ti/TiAlN multilayer coatings eroded by the glass beads started at the metallic macroparticles. Cracks and delamination were generated due to the incoordinate deformation between the substrate and the coating under the erodent impacting. Cracks and delamination would further develop under continuous erosion. The coatings failed finally under the joint actions of the delamination and radial cracks. The failure of the Ti/TiAlN multilayer coatings eroded by the glass beads showed the feature of the "piece by piece" mechanism. The Ti layers and interfaces deflected the propagation of the radial cracks, limiting the extension of the lateral cracks.

3.4.3. General discussion

The erodent affected the erosion resistance of the Ti/TiAlN multilayer coatings by making an influence on their erosion behavior and failure mechanism.

In this study, the silica sand was hard and small (~61 μm) with sharp edges, whereas the glass beads were soft and blunt although they were larger (~106 μm). The pressure of the compressed air was the same for all tests, i.e., the initial kinetic energy of all erodent was the same. When the silica sand impacted the surface of the Ti/TiAlN multilayer coatings, cracks formed at a TiAlN layer due to the strong erosive effect of the silica sand on the coatings. But the cracks were hindered by the adjacent Ti layers and the formed interfaces, followed by the newly exposed TiAlN starting to be eroded. Most of the kinetic energy was released by cracking the exposed TiAlN layer rather than transferring it to the substrate. Therefore, the coating exhibited the "layer by layer" failure mechanism when hit by the silica sand. According to the study by Deng [4], the TiAlN monolithic coatings were removed from the substrate in the form of small fragments due to repeated attacks by the erosion particles. The coatings worn gradually with the erosion lasting, and eventually leading to the substrate exposure. During this procedure, cracking and removal of the partial coating, all results in redistribution of the contact pressures and overstressing around the damaged areas that facilitate the further coating damage. After reaching the critical size under repetitive impacts, the large chip may remove from the surface. In this study, The Ti/TiAlN-3 exhibited a similar hardness of the TiAlN monolithic coatings, with the induced Ti layers, Ti/TiAlN-3 showed a higher crack resistance than that of the TiAlN monolithic coating, enhancing the erosion resistance of the coatings. However, the erosion rate sharply increased with the number of cycles increasing because the thickness of the TiAlN layer, as well as the hardness and crack resistance, declined as the number of cycles was increased. This led to the decline of the erosion resistance of the TiAlN layer and accelerating the process of "layer by layer" erosion.

Compared to the silica sand, the glass beads were less erosive, whose kinetic energy was transferred to the substrate by the coatings greatly. And the coatings absorbed the energy through plastic deformation, resulting in lateral cracks and delamination between the coating and the substrate. Combined with the formation of the radial cracks at the edge of the pits leading to the coatings. The erosion rates of the Ti/TiAlN multilayer coatings did not change significantly with the variation of the number of cycles since the delamination played the leading role in the failure of the coating, although the radial cracks were deflected by the Ti layers and interfaces.

4. Conclusion

In this work, Ti/TiAlN multilayer coatings with the different cycles were deposited on Ti–6Al–4V substrates by a home-made hybrid multisource cathodic arc ion deposition system. The effects of the silica sand and glass beads on erosion behavior of the coatings were investigated. Results showed that the Ti/TiAlN multilayer coatings exhibited the "layer by layer" failure mechanism when eroded by the silica sand, and erosion rate dramatically increased with the increasing the number of cycles, owing to the deterioration of the coatings' mechanical properties. However, the erosion rate of the coatings treated by glass beads was independent of the number of cycles, where the coating failure was dominated by the "piece by piece" failure mechanism. The Ti layers and interfaces enhanced the erosion resistance of coatings by hindering the propagation of radial cracks and restraining the lateral cracks within one single TiAlN layer. The erosion resistance of coatings depends on their comprehensive mechanical properties like high hardness, strong adhesion strength and good crack resistance. Under the premise of

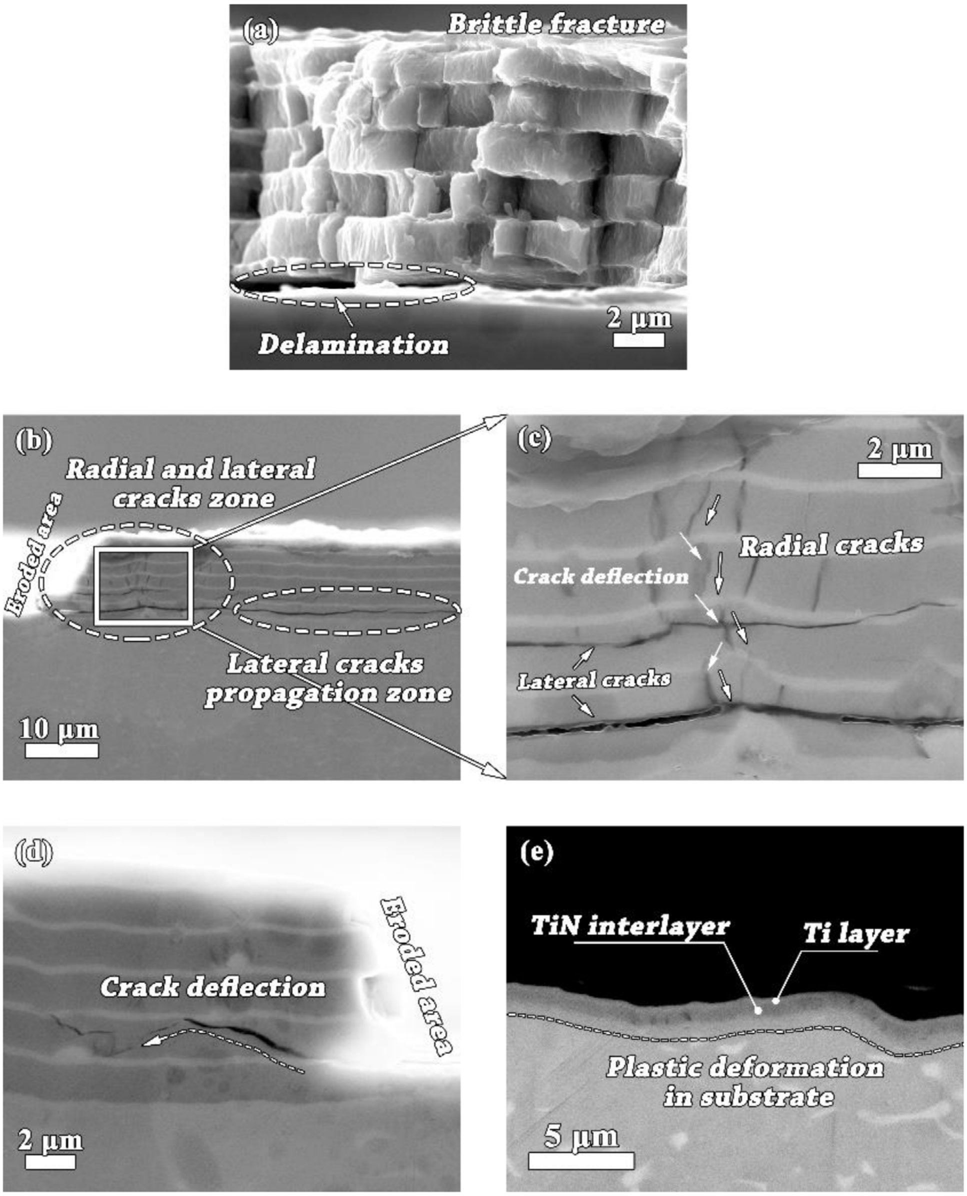

Fig. 12. Cross-sectional morphology of the Ti/TiAlN-6 eroded by glass beads. SEM image of (a) unpolished cross-sectional erosion scare, (b) polished cross-sectional erosion scare, (c) enlarged image of the framed area in (b), (d) deflection of the lateral crack, (e) development of the pit and (f) plastic deformation at the substrate.

high hardness, enhancing the adhesion strength and crack resistance of the coatings is a promising route to obtain coatings with excellent erosion resistance.

Acknowledgements

This work was financially supported by the National Science and Technology Major Project (No. 2017-VII-0012-0108), CAS Interdisciplinary Innovation Team (No. 292020000008), and K. C. Wong Education Foundation (No. GJTD-2019-13).

References

[1] E. Bousser, L. Martinu, J.E. Klemberg-Sapieha, Surf. Coat. Technol. 257 (2014) 165–181.
[2] J. Lin, R. Wei, F. Ge, Y. Li, X. Zhang, F. Huang, M. Lei, Surf. Coat. Technol. 336 (2018) 106–116.
[3] D. Eichner, A. Schlieter, C. Leyens, L. Shang, S. Shayestehaminzadeh, J.M. Schneider, Wear 402-403 (2018) 187–195.
[4] J. Deng, F. Wu, Y. Lian, Y. Xing, S. Li, Int. J. Refract. Met. Hard Mater. 35 (2012) 10–16.
[5] R. Wei, E. Langa, J. Arps, Q. Yang, L. Zhao, Plasma Process. Polym. 4 (2007) S693–S699.
[6] Q. Yang, D.Y. Seo, L.R. Zhao, X.T. Zeng, Surf. Coat. Technol. 188 (2004) 168–173.
[7] H. Zhang, Z. Li, W. He, B. Liao, G. He, X. Cao, Y. Li, Surf. Coat. Technol. 353 (2018) 210–220.
[8] Z. Wang, D. Zhang, P. Ke, X. Liu, A. Wang, J. Mater. Sci. Technol. 31 (2015) 37–42.
[9] J. Shuai, X. Zuo, Z. Wang, P. Guo, B. Xu, J. Zhou, A. Wang, P. Ke, Ceram. Int. 46 (5) (2020) 6672–6681.
[10] P. Wieciński, J. Smolik, H. Garbacz, K.J. Kurzydlowski, Vacuum 107 (2014) 277–283.
[11] D.A. Colombo, A.D. Mandri, M.D. Echeverria, J.M. Massone, R.C. Dommarco, Thin Solid Films 647 (2018) 19–25.
[12] A. Khoddami, D. Salimi-Majd, B. Mohammadi, Surf. Coat. Technol. 372 (2019) 173–189.
[13] L.A. Dobrzański, K. Lukaszkowicz, J. Mater. Process. Technol. 157-158 (2004) 317–323.
[14] L.A. Dobrzański, K. Lukaszkowicz, A. Križ, J. Mater. Process. Technol. 143-144 (2003) 832–837.
[15] W. Tillmann, E. Vogli, S. Momeni, Vacuum 84 (2009) 387–392.
[16] E. Vogli, W. Tillmann, U. Selvadurai-Lassl, G. Fischer, J. Herper, Appl. Surf. Sci. 257 (2011) 8550–8557.
[17] S. Lin, K. Zhou, M. Dai, E. Lan, Q. Shi, F. Hu, T. Kuang, C. Zhuang, Vacuum 122 (2015) 179–186.

[18] X. Cao, W.F. He, B. Liao, H. Zhou, H.H. Zhang, C. Tan, Z.F. Yang, Surf. Coat. Technol. 365 (2019) 214–221.
[19] B. Borawski, J. Singh, J.A. Todd, D.E. Wolfe, Wear 271 (11-12) (2011) 2782–2792.
[20] R. Jiang, M. Li, Y. Yao, J. Guan, H. Lu, Front. Mater. Sci. 13 (2019) 107–125.
[21] A.C. Fischer-Cripps, Nanoindentation, third ed., Springer, New York, 2011, pp. 147–155.
[22] W.C. Oliver, G.M. Pharr, J. Mater. Res. 7 (2011) 1564–1583.
[23] G. Greczynskia, L. Hultmana, M. Odén, Surf. Coat. Technol. 374 (2019) 923–934.
[24] C. Badinia, S.M. Deambrosisb, O. Ostrovskayaa, V. Zinb, E. Padovanoa, E. Miorinb, M. Castellinoc, S. Biamino, Ceram. Int. 43 (2017) 5417–5426.
[25] J.F. Marco, J.R. Gancedo, M.A. Auger, O. Sanchez, J.M. Albella, Surf. Interface Anal. 37 (2005) 1082–1091.
[26] R. Ananthakumar, B. Subramanian, A. Kobayashi, M. Jayachandran, Ceram. Int. 38 (2012) 477–485.
[27] P. Wieciński, J. Smolik, H. Garbacz, K.J. Kurzydłowski, Surf. Coat. Technol. 240 (2014) 23–31.
[28] V. Bonu, M. Jeevitha, V.P. Kumar, S. Bysakh, H.C. Barshilia, Appl. Surf. Sci. 478 (2019) 872–881.
[29] S. Hassani, J.E. Klemberg-Sapieha, L. Martinu, Surf. Coat. Technol. 205 (2010) 1426–1430.
[30] V.P. Swaminathan, R.H. Wei, D.W. Gandy, J. Eng. Gas. Turb. Power. 132 (8) (2010).
[31] D.E. Wolfe, B.M. Gabriel, M.W. Reedy, Surf. Coat. Technol. 205 (2011) 4569–4576.
[32] X. Cao, W. He, G. He, B. Liao, H. Zhang, J. Chen, C. Lv,Surf. Coat. Technol. 378 (2019), 125009.
[33] J. Chen, M. Geng, Y. Li, Z. Yang, Y. Chai, G. He, Coatings 9 (2019) 11.
[34] E. Bousser, M. Benkahoul, L. Martinu, J.E. Klemberg-Sapieha, Surf. Coat. Technol. 203 (2008) 776–780.
[35] P. Wiecinski, J. Smolik, H. Garbacz, J. Bonarski, A. Mazurkiewicz, K.J. Kurzydlowski, Surf. Coat. Technol. 309 (2017) 709–718.
[36] J. Di, S.S. Wang, L. Zhang, L.X. Cai, Y.H. Xie, Surf. Coat. Technol. 333 (2018) 115–124.
[37] P.J. Burnett, D.S. Rickerby, Thin Solid Films 154 (1987) 403–416.
[38] H. Ichimura, A. Rodrigo, Surf. Coat. Technol. 126 (2000) 152–158.
[39] Y. Xie, H.M. Hawthorne, Surf. Coat. Technol. 155 (2002) 121–129.
[40] S. Zhang, D. Sun, Y.Q. Fu, H.J. Du, Surf. Coat. Technol. 198 (2005) 74–84.
[41] E. Bousser, L. Martinu, J.E. Klemberg-Sapieha, J. Mater. Sci. 48 (2013) 5543–5558.
[42] X. Xu, F. Su, Z. Li, Wear 430-431 (2019) 67–75.
[43] X. Cai, Y. Gao, F. Cai, L. Zhang, S. Zhang, Appl. Surf. Sci. 483 (2019) 661–669.
[44] K. Weicheng, S. Hui, K. Dejun, J. Tribology 140 (2018) 041301, 9.
[45] W.D. Münz, D.B. Lewis, S. Creasey, T. Hurkmans, T. Trinh, W. Ijzendorn, Vacuum 46 (1995) 323–330.